Indonesian Journal of Electrical Engineering and Computer Science
Vol. 42, No. 2, May 2026, pp. 572∼583
ISSN: 2502-4752, DOI: 10.11591/ijeecs.v42.i2.pp572-583

Pomelo maturity classification from field-acquired images using oil-gland morphology and a rule-based image-processing pipeline

Sopapun Suwansawang[1], Harutai Dinsakul[1], Wirot Buangam[1], Jiraroj Tosasukul[2]
[1]Department of Electrical Engineering, Faculty of Science and Technology, Nakhon Pathom Rajabhat University (NPRU), Nakhon Pathom, Thailand
[2]Department of Mathematics, Faculty of Science, Naresuan University (NU), Phitsanulok, Thailand

Article Info

Article history:

Received Dec 30, 2025
Revised Feb 24, 2026
Accepted May 26, 2026

Keywords:

Non-destructive classification
Oil gland detection
Pomelo maturity
Rule-based image processing
Surface feature analysis

ABSTRACT

Pomelo maturity assessment in commercial orchards relies predominantly on visual inspection and harvest age records, which introduce inconsistency in post-harvest grading. Non-destructive alternatives such as near-infrared spectroscopy and acoustic sensing have been reported, but typically require specialised instruments and controlled acquisition conditions. This study investigates the feasibility of oil-gland morphology as an interpretable maturity indicator, implemented as a rule-based image-processing pipeline executable on standard CPU hardware without model training. A hierarchical rule-based framework was developed to classify pomelo maturity from gland count features extracted under natural outdoor illumination. Thirty-three Citrus maxima samples (Khao Yai cultivar) representing three maturity stages were analysed in this proof-of-concept study ($n = 11$ per stage). The pipeline integrates adaptive thresholding, subregion segmentation, multi-scale morphological detection, and threshold-based classification. Detection reliability was verified on synthetic dot-pattern images prior to real-sample evaluation. On the collected dataset, the framework achieved an overall accuracy of 78.8% with a macro-averaged F1-score of 0.784. No misclassification occurred between the immature and mature groups; errors arose exclusively between adjacent stages. Mean processing time was 57 seconds per image on a consumer-grade laptop. Given the limited sample size and single-cultivar scope, these results represent methodological feasibility rather than validated generalisation, and establish a baseline for morphology-based maturity assessment in pomelo.

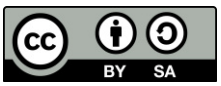

Corresponding Author:

Sopapun Suwansawang
Department of Electrical Engineering, Faculty of Science and Technology
Nakhon Pathom Rajabhat University
85 Malaiman, Nakhon Pathom 43000, Thailand
Email: sopapun@webmail.npru.ac.th

1. INTRODUCTION

Field-deployable computer vision systems in agriculture must operate under uncontrolled illumination, heterogeneous backgrounds, and limited computational resources. Deep learning has substantially advanced automated fruit maturity assessment through convolutional neural networks and transformer-based architectures [1], [2], achieving strong predictive performance across diverse crops [3]. However, these systems

typically require large labeled datasets, extensive training, and hardware capable of real-time inference [4]-[6]. Spectral and hyperspectral imaging methods offer complementary biochemical information but depend on specialized equipment and calibration procedures [1]. Together, these constraints motivate continued interest in computationally efficient, interpretable frameworks based on conventional RGB imaging.

Pomelo (Citrus maxima) maturity assessment is a representative example of this challenge. Harvest timing in commercial orchards is commonly determined through visual inspection and fruit age records, with growers relying on subjective surface cues including peel color and oil gland appearance. These indicators lack standardized quantitative procedures [7], reflecting the broader absence of objective, automated systems capable of reliable operation under natural field conditions.

Oil glands embedded in the citrus flavedo layer form discrete surface structures that undergo developmental changes during fruit growth [8]. Machine vision has been widely applied across citrus production tasks including grading and harvest identification [9], with oil gland surface appearance demonstrated as a functional feature for non-destructive citrus quality assessment from digital images [10]. For pomelo specifically, the visual contrast between oil glands and surrounding peel tissue has been identified as a discriminative feature in multi-parameter maturity evaluation [7], [11]. Despite this relevance, explicit spatial quantification of oil-gland morphology within a deterministic, rule-based classification framework has received limited systematic investigation.

As summarized in Table 1, representative maturity detection approaches involve trade-offs among predictive capability, computational demand, and deployment complexity. This study investigates the feasibility of using oil-gland morphology as an interpretable maturity indicator through a rule-based image-processing pipeline designed for operation on standard CPU hardware under practical field acquisition conditions. The framework integrates preprocessing, subregion segmentation, morphological filtering, and empirical decision rules within an OpenCV-based pipeline, emphasizing deterministic decision logic over data-intensive learning strategies.

Table 1. Comparison of representative fruit maturity detection approaches. Characteristics reflect intrinsic methodological properties; direct accuracy comparisons across datasets are not intended

Approach	Computational demand and transparency	Deployment characteristics
Spectral imaging [1]	Moderate–high; moderate feature interpretability	Specialised hardware; calibration required
Deep learning [4], [6]	High; limited decision interpretability	Strong in controlled settings; large labelled dataset required
Proposed rule-based pipeline	Low-to-moderate; no GPU or specialist hardware required; explicit traceable decision logic	Standard RGB camera; platform-independent; no training data required

Image acquisition was performed using consumer-grade RGB devices, and the processing framework is platform-independent with no device-specific calibration required. The objective is to establish a methodological baseline for morphology-based pomelo surface analysis under practical field conditions rather than to compete directly with high-capacity data-driven models.

The main contributions are as follows:

- Formulation of a morphology-based maturity framework grounded in spatial characteristics of oil glands on pomelo peel surfaces.
- A deterministic OpenCV-based pipeline integrating preprocessing, subregion segmentation, morphological filtering, and rule-based decision logic.
- Dual-stage validation combining field-collected pomelo images with synthetic dot-pattern experiments to evaluate geometric detection behavior independently of biological variability.

Given the limited dataset and single-cultivar scope, this work is positioned as a proof-of-concept baseline rather than a generalized prediction model, providing an engineering reference point for morphology-based surface analysis in low-cost agricultural vision systems.

2. MATERIALS AND METHODS

The proposed approach employs a deterministic image-processing pipeline to quantify oil-gland morphology on pomelo peel surfaces and classify fruit maturity stages. The framework was designed to provide an interpretable, training-free solution executable on standard CPU hardware, suitable for practical agricultural environments where controlled acquisition conditions and large labelled datasets are not available [12].

The workflow consists of four sequential stages: (i) image acquisition and preprocessing, (ii) segmentation and oil-gland detection, (iii) spatial feature extraction and feature analysis, and (iv) rule-based maturity classification, as illustrated in Figure 1.

Pomelo images were first acquired under natural illumination and processed through grayscale conversion, Gaussian smoothing, adaptive thresholding [13], and morphological filtering [14] to enhance oil-gland structures while suppressing background noise. Each image was divided into smaller subregions to reduce the influence of peel curvature during detection. Oil glands were subsequently identified using a multi-scale convolution-based detection strategy [15]. Detected glands were analysed to extract spatial features including centroid coordinates and inter-gland distances. Finally, fruit maturity was determined using a hierarchical deterministic rule derived from observed oil-gland count statistics.

All algorithms were implemented in Python 3.10 using OpenCV 4.5 for image-processing operations and NumPy for numerical computation. Experiments were executed on a laptop computer equipped with an Intel Core i7 processor.

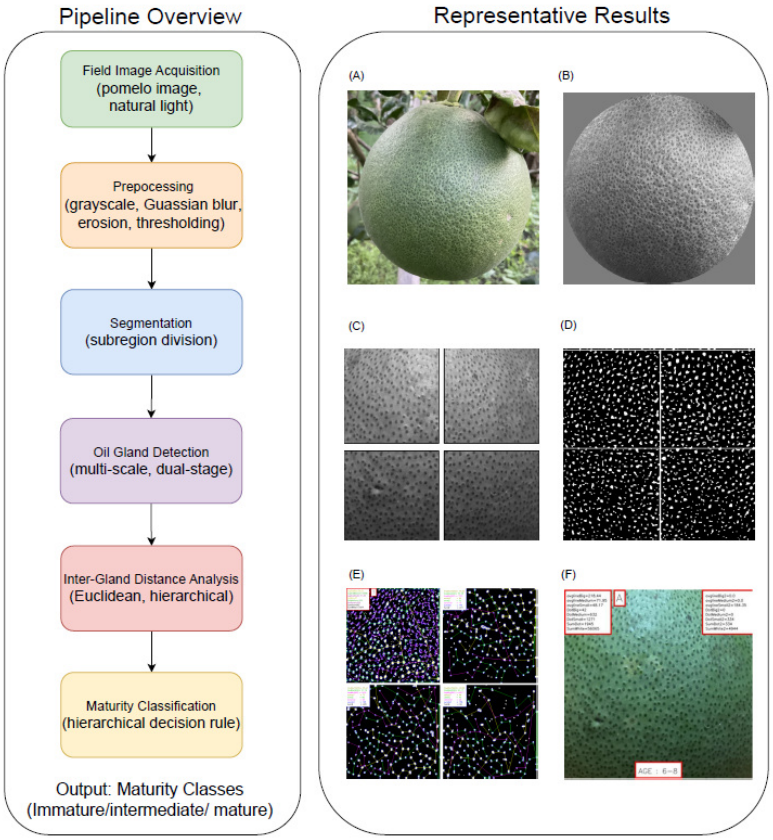

Figure 1. Proposed pipeline for pomelo maturity classification. Left: processing stages — (A) raw image, (B) grayscale conversion, (C) subregion segmentation, (D) adaptive thresholding and morphological filtering, (E) multi-scale oil-gland detection with centroid extraction, and (F) classification output with detected gland overlay and maturity label right: representative results for each stage

2.1. Image acquisition and preprocessing

A total of 33 Citrus maxima (Khao Yai cultivar) pomelo samples were collected, representing three maturity stages: 1–3 months, 4–5 months, and 6–8 months post-anthesis. Each maturity group comprised

11 samples to maintain balanced class representation. Given the exploratory nature of this feasibility study, the dataset size is consistent with pilot-scale morphological assessments reported in the literature [10].

Samples at the 1–3 and 4–5 months stages were photographed on-tree in the orchard under natural outdoor illumination. Samples at the 6–8 months stage were collected following harvest — standard commercial practice for this cultivar, in which mature fruit is detached to allow post-harvest conditioning that improves flavour development — and photographed at an on-site storage facility under natural ambient illumination without controlled lighting or calibration panels. No controlled lighting conditions or calibration panels were employed at any stage; all images are therefore classified as field-acquired. Images were captured using consumer-grade RGB devices (iPhone SE and iPad Air 9th generation, 12 MP rear cameras) [16].

Each image was manually cropped to 600×600 pixels and converted to grayscale. Gaussian smoothing with a 5×5 kernel was applied to suppress high-frequency noise while preserving gland boundaries, consistent with preprocessing approaches used in citrus surface analysis [16].

Image binarization was performed using adaptive Gaussian thresholding with block size 11 and constant $C = 1$ under the `THRESH_BINARY_INV` configuration. Adaptive thresholding was selected over global thresholding [17] to accommodate local illumination variation across the peel surface [12], [13]. Morphological filtering was subsequently applied using a 2×2 structuring element: erosion (two iterations) followed by dilation (one iteration), to remove small artefacts while preserving gland structures [10], [14].

2.2. Segmentation and oil-gland detection

To reduce spatial variability introduced by peel surface curvature, each 600×600 pixel image was divided into four 300×300 pixel subregions, as shown in Figure 1(C). Processing smaller local patches mitigates the effect of uneven peel geometry on binarization consistency.

Oil glands were detected using a multi-scale convolution-based procedure designed to capture structures of varying sizes, corresponding to stage (E) in Figure 1. In the first detection pass, convolution kernels of sizes 3×3, 5×5, and 7×7 were applied sequentially. The use of multiple kernel scales follows the principle that surface structures of different sizes require correspondingly scaled detection operators [12], [15]. Candidate regions exceeding empirically defined intensity thresholds were identified as gland structures using connected-component analysis [18] and masked to prevent repeated detections across kernel scales.

A second detection pass was performed on upscaled subregions using bilinear interpolation to improve sensitivity to smaller gland structures, particularly relevant for distinguishing earlier maturity stages.

Detected gland regions were categorised into three size groups (small, medium, and large) based on relative area ranges observed within the dataset.

2.3. Spatial feature extraction

Pairwise Euclidean distances between detected gland centroids were computed within each subregion, yielding a symmetric distance matrix $\mathbf{D} \in \mathbb{R}^{N\times N}$, where N denotes the number of detected glands. The computational complexity of this operation is $O(N^2)$.

Mean inter-gland distance was calculated separately for each size group. For large glands:

$$\bar{d}_L = \frac{2}{n_L(n_L-1)} \sum_{1\le i<j\le n_L} d_{i,j}, \tag{1}$$

where n_L is the number of detected large glands and $d_{i,j}$ is the Euclidean distance between gland centroids i and j. Equivalent formulations were applied to medium ($\bar{d}_M$) and small ($\bar{d}_S$) gland groups.

The nearest-neighbour distance for each gland i was defined as:

$$d_{i,\mathrm{nn}} = \min_{j\neq i} d_{i,j}. \tag{2}$$

together, $\bar{d}$ and $d_{i,\mathrm{nn}}$ characterise global spacing and local clustering behaviour of oil glands across the peel surface, respectively.

2.4. Feature analysis and threshold selection

Both inter-gland distance descriptors ($\bar{d}_L$, $\bar{d}_M$, $\bar{d}_S$, $d_{i,\mathrm{nn}}$) and gland count statistics were examined as candidate classification features. Inspection of the collected dataset revealed that gland count variables — particularly the number of large glands (n_L) and the number of small glands in the second detection pass

(n_S) — exhibited more consistent separation between maturity groups than distance-based descriptors under the present acquisition conditions. Distance features showed overlapping distributions across stages and were therefore not incorporated into the final decision rule. Their computation nonetheless contributes to the morphological characterisation reported in this study and may serve as additional discriminative features in future work with larger datasets.

2.5. Rule-based maturity classification

The classification rule was constructed from the two gland count features identified in the preceding analysis, n_L and n_S, on the basis of their observed group separation in the dataset, as illustrated in Figure 2.

Primary criterion — large gland count (n_L). Figure 2(A) shows the distribution of n_L across the three maturity stages. The 6–8 month group produced consistently higher counts (range: 29–178) than the 4–5 month group (range: 0–23). The threshold $n_L^* = 40$ was selected as the lowest value that maximises separation between the mature group and the two earlier stages in the collected dataset. It is noted that two samples in the 6–8 month group (Samples 4 and 5; $n_L = 29$) fell below this threshold, and three samples in the 1–3 month group (Samples 6, 10, and 11; $n_L = 56$, 80, and 94) exceeded it. These overlaps are acknowledged as a limitation of the count-based rule under the present dataset size and acquisition conditions.

Secondary criterion — small gland count (n_S). For samples classified as non-mature under the primary criterion ($n_L \leq 40$), Figure 2(B) shows that n_S from the second detection pass provided further separation between the 1–3 month group (range: 125–308) and the 4–5 month group (range: 0–317). The threshold $n_S^* = 156$ was selected from the observed distribution. One sample in the 4–5 month group (Sample 11; $n_S = 317$) exceeded this threshold, representing a potential misclassification under the secondary criterion.

The complete classification procedure is summarised in Algorithm 1.

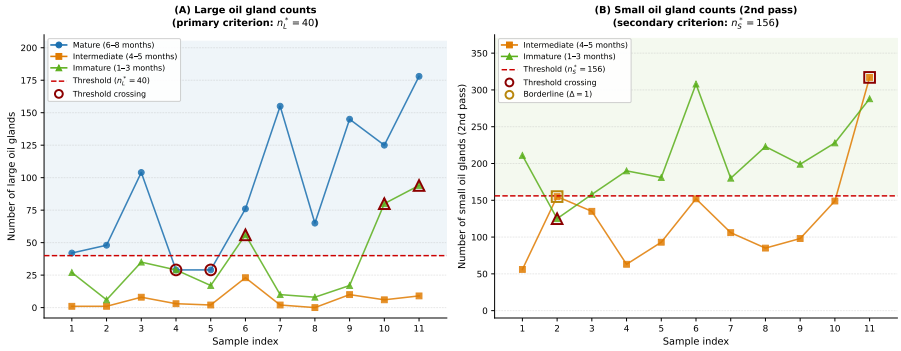

Figure 2. Oil gland count distributions across maturity stages ($n = 11$ per stage, Khao Yai cultivar). (A) large gland counts with primary threshold $n_L^* = 40$; circled markers indicate samples crossing the threshold. (B) small gland counts (second detection pass) with secondary threshold $n_S^* = 156$. Thresholds are empirical and cultivar-specific

Algorithm 1 Hierarchical maturity classification rule

Require: n_L: large gland count; n_S: small gland count (second pass)
1: **if** $n_L > 40$ **then**
2: **Output:** Mature (6–8 months)
3: **else if** $n_S < 156$ **then**
4: **Output:** Intermediate (4–5 months)
5: **else**
6: **Output:** Immature (1–3 months)
7: **end if**

The thresholds $n_L^* = 40$ and $n_S^* = 156$ were selected by inspection of the observed count distributions and are specific to the Khao Yai cultivar under the described acquisition conditions. The overall classification accuracy achieved by this rule on the collected dataset is reported in section 3. Given the limited sample size ($n = 11$ per stage) and single-cultivar scope, these thresholds represent cultivar-specific empirical parameters of a proof-of-concept feasibility study rather than statistically optimised classification criteria.

3. RESULTS

The pipeline was evaluated in two stages: first on synthetic images to validate detection reliability, then on the collected Khao Yai pomelo dataset to assess morphological characterisation and maturity classification performance.

3.1. Algorithm validation on synthetic data

Detection reliability was assessed on 100 synthetically generated images prior to real-image evaluation (Figure 3). Each image contained precisely placed dot patterns representing 30 small, 20 medium, and 10 large gland structures, distributed randomly to simulate natural spatial variability.

Size-specific detection accuracies were 98.7% for large, 95.9% for medium, and 95.4% for small glands, yielding an overall detection rate of 96.1%. Detection errors occurred at sites of spatial overlap, where adjacent structures merged or smaller ones were occluded by larger neighbours, consistent with known limitations of morphological-filtering approaches in dense regions [10], [12]. These results confirmed sufficient detection reliability to proceed with real-image evaluation.

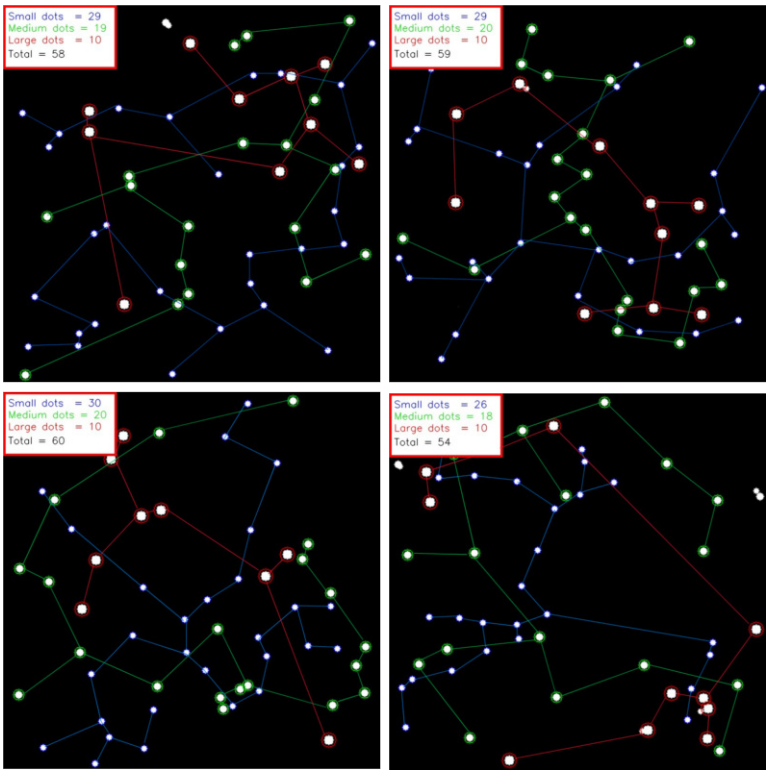

Figure 3. Representative synthetic test images used for algorithm validation. Each panel shows detected gland structures colour-coded by size: small (blue), medium (green), and large (red circles). Ground-truth counts were 30 small, 20 medium, and 10 large per image; detected totals ranged from 57 to 60, reflecting the overlap-induced errors described in the text

3.2. Morphological feature characterisation

Descriptive statistics for inter-gland distance and gland count features, computed according to the spatial feature extraction described in section 2, are reported for correctly classified samples in Table 2. The subset comprises $n = 7$, 10, and 9 samples for the 1–3, 4–5, and 6–8 month groups, respectively; misclassified samples were excluded because their feature values deviated from the group-level distributions on which the rule was derived, and their inclusion would conflate classification-rule performance with morphological characterisation. The classification behaviour of all 33 samples, including misclassified cases, is fully documented in section 3.3 and Figure 4.

Three observations are notable. First, medium gland inter-gland distances were highly stable across all maturity stages ($CV < 5\%$), indicating that medium gland spacing is structurally invariant during pomelo development and is therefore not useful as a discriminative feature in its own right. Second, large gland counts increased approximately fivefold from the 1–3 month group (20.43 ± 10.14) to the 6–8 month group (104.22 ± 49.36), consistent with progressive oil gland differentiation during citrus fruit maturation [8], [19]. Third, small gland counts from the first detection pass declined from 2332.71 ± 284.11 to 1629.22 ± 204.51 across the same interval, suggesting concurrent structural remodelling of smaller gland units, a pattern noted in broader citrus peel development studies [8]. The 4–5 month group exhibited the highest variability in large gland count ($CV = 124.06\%$), reflecting the biological heterogeneity expected during a transitional developmental stage [19].

Table 2. Summary statistics (mean ± SD; CV %) of inter-gland distances and oil gland counts for correctly classified samples across maturity stages ($n = 7$, 10, and 9 for the 1–3, 4–5, and 6–8 month groups, respectively). Distance values are in pixels

Feature	1–3 months	4–5 months	6–8 months
Large dist. (px)	219.63 ± 67.31 (30.65)	98.50 ± 128.20 (130.15)	128.40 ± 41.46 (32.29)
Medium dist. (px)	54.12 ± 2.44 (4.51)	54.59 ± 1.84 (3.38)	54.22 ± 2.01 (3.71)
Small dist. (px)	30.65 ± 2.34 (7.63)	33.06 ± 1.06 (3.20)	32.76 ± 1.81 (5.53)
Large count	20.43 ± 10.14 (49.59)	5.60 ± 6.94 (124.06)	104.22 ± 49.36 (47.35)
Medium count	508.43 ± 45.16 (8.88)	474.70 ± 138.51 (29.18)	640.67 ± 56.57 (8.83)
Small count (1st pass)	2332.71 ± 284.11 (12.18)	2262.80 ± 277.19 (12.25)	1629.22 ± 204.51 (12.55)
Small count (2nd pass)	191.71 ± 21.58 (11.26)	109.20 ± 36.71 (33.62)	227.33 ± 83.06 (36.54)

3.3. Classification performance

Applying the hierarchical rule (Algorithm 1) to all 33 collected samples yielded an overall accuracy of 78.79% (26/33). Class-wise results, derived from the confusion matrix in Figure 4, are summarised in Table 3.

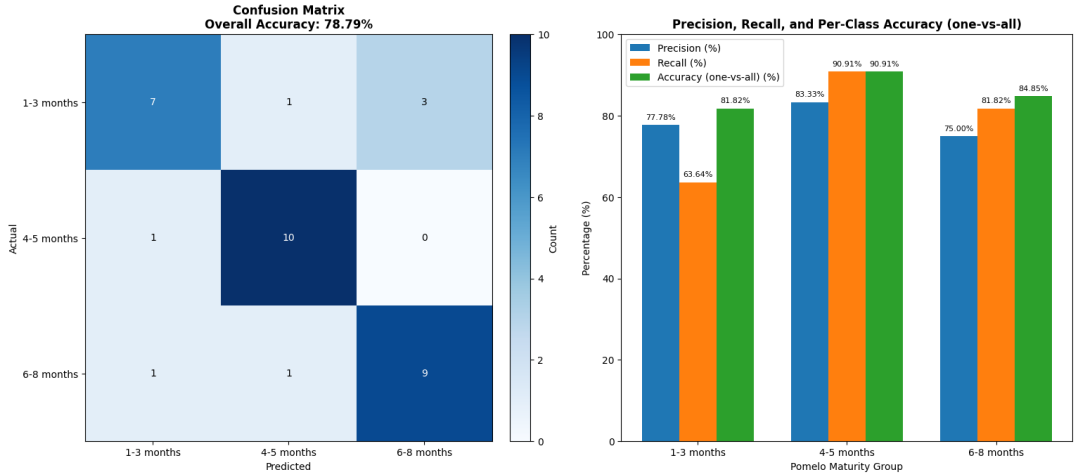

Figure 4. Left: confusion matrix for the hierarchical rule-based classifier applied to 33 Khao Yai pomelo samples (overall accuracy: 78.79%). Right: precision, recall, and one-vs-all accuracy per maturity group

Table 3. Class-wise evaluation metrics derived from the confusion matrix in Figure 4. The macro-averaged F1-score is reported in the final row as the unweighted mean of the three class-wise F1-scores [20], [21]

Group	TP	FP	FN	Prec. (%)	Rec. (%)	F1
1–3 months	7	2	4	77.78	63.64	0.700
4–5 months	10	2	1	83.33	90.91	0.870
6–8 months	9	3	2	75.00	81.82	0.783
Macro average						*0.784*

The macro-averaged F1-score of 0.784 was computed as the unweighted mean of the three class-wise F1-scores following the formulation in Sokolova and Lapalme [20]. Since the present dataset is class-balanced ($n = 11$ per stage), the macro-averaged and weighted F1-scores are numerically equivalent; the macro average is reported as it treats each maturity class equally regardless of class size [20], [21]. For balanced multiclass datasets, the F1-score has been shown to provide a more informative summary of classifier performance than overall accuracy alone [20], [22]. Precision, recall, and F1-score were computed from the per-class confusion matrix entries using standard definitions [20].

The 4–5 month group achieved the highest F1-score (0.870) and recall (90.91%), reflecting strong separation under the secondary criterion $n_S^* = 156$. The 1–3 month group yielded the lowest recall (63.64%), attributable to the three samples (S6, S10, and S11) whose large gland counts exceeded the primary threshold $n_L^* = 40$, as documented in section 2. Importantly, no sample from the 1–3 month group was misclassified as mature (6–8 months), nor vice versa: all misclassifications involved adjacent maturity stages only. This result indicates that the pipeline correctly captures the largest developmental contrast between immature and mature fruit, consistent with the progressive oil gland differentiation reported in citrus peel studies [8], [10].

3.4. Computational cost

The mean processing time per image was 57 seconds, measured on an Intel Core i7 laptop computer (Python 3.10, OpenCV 4.5, single-threaded CPU execution, $n = 33$ samples), encompassing the complete pipeline from preprocessing to classification output. No GPU acceleration was employed.

The processing time is primarily attributable to the iterative structure of the detection stage, which applies convolution kernels of three scales (3×3, 5×5, and 7×7) sequentially in the first pass, followed by a second detection pass on upscaled subregions to capture smaller gland structures. Each pass involves per-subregion masking and candidate verification, resulting in repeated traversals over the image content before a classification decision is reached. This deliberate multi-pass design prioritises detection completeness over processing speed, consistent with the proof-of-concept objectives of this study.

While the current implementation precludes real-time field deployment, the pipeline requires no model training, labelled datasets, or specialist inference infrastructure. Computational efficiency could be improved in future work through kernel parallelisation or replacing the exhaustive multi-pass strategy with a single-pass learned detector, without altering the interpretable rule-based classification stage [12].

3.5. Statistical validation

The consistency of group-level performance was assessed using the one-sided exact binomial test [23], with the null hypothesis that each group's true classification accuracy is no lower than the overall observed accuracy of the full dataset ($p_0 = 0.7879$):

$$H_0 : p \geq p_0,$$
$$H_1 : p < p_0. \tag{3}$$

This formulation tests whether any individual group performs significantly worse than the dataset-level average. p-values were computed from the exact binomial probability mass function; two-sided Clopper–Pearson 95% confidence intervals were reported as a complementary measure of uncertainty [23].

Results are presented in Table 4. No group returned a p-value below $\alpha = 0.05$, indicating that the null hypothesis was not rejected for any group. The 1–3 month group showed the widest confidence interval [0.308, 0.891], reflecting the lower number of correct classifications ($k = 7$ of 11) combined with the small per-group sample size. These results are consistent with stable group-level performance within the present dataset; they should not be interpreted as evidence of generalisation beyond the Khao Yai cultivar or the described acquisition conditions, given the limited sample size and single-cultivar scope [10].

Table 4. One-sided exact binomial test results per maturity group. H_0: group accuracy $\geq p_0 = 0.7879$; $\alpha = 0.05$. Two-sided Clopper–Pearson 95 % CIs are shown

Group	Lower CI	Upper CI	p-value
1–3 months	0.308	0.891	0.189
4–5 months	0.587	0.998	0.927
6–8 months	0.482	0.977	0.712

4. DISCUSSION

4.1. Interpretation of classification performance

The overall accuracy of 78.79% and macro-averaged F1-score of 0.784 are consistent with the exploratory scope of this study. All misclassifications occurred between adjacent maturity stages; no sample from the 1–3 month group was misclassified as mature, nor vice versa. This result indicates that the pipeline correctly captures the most pronounced developmental contrast in oil-gland morphology, consistent with the progressive gland differentiation described in citrus peel studies [8], [10]. The lower recall of the 1–3 month group (63.64%) reflects the overlap in large gland counts between early-stage and transitional samples, which is a known source of difficulty in rule-based maturity assessment under biological variability [19].

The intermediate group (4–5 months) achieved the highest F1-score (0.870), consistent with the distinct morphological characteristics observed during the transitional developmental phase. The wide confidence interval for the 1–3 month group [0.308, 0.891] reflects both the lower classification accuracy and the inherent uncertainty associated with small per-group sample sizes [23]. These results should be interpreted within the constraints of a proof-of-concept study rather than as evidence of generalisation beyond the present cultivar and acquisition conditions.

4.2. Contributions relative to prior work

This study presents a transparent, rule-based pipeline that quantifies oil-gland count and spatial morphology from field-acquired images without requiring model training, labelled datasets, or specialist sensing equipment. In contrast to spectroscopic and acoustic methods [1], the proposed approach relies solely on consumer-grade RGB imaging under natural illumination. Compared with deep learning classifiers [4], [6], the rule-based framework offers explicit decision traceability at the cost of reduced predictive capacity.

Medium gland inter-gland distances demonstrated exceptional stability across all maturity stages ($CV < 5\%$), suggesting that medium gland spacing is structurally invariant during pomelo development. This finding is consistent with the developmental biology of citrus flavedo tissue reported in the literature [8] and represents a novel morphometric observation for the Khao Yai cultivar. The synthetic dot-pattern validation, which achieved an overall detection rate of 96.1%, provides a geometry-independent baseline for the detection algorithm that is decoupled from biological variability. This dual-stage validation design strengthens confidence in algorithmic behaviour prior to real-sample deployment [10], [12].

4.3. Limitations

Several limitations constrain the scope of the present findings:

- Dataset size and cultivar scope. The dataset of 33 samples from a single cultivar (Khao Yai) limits statistical power and generalisability. The derived thresholds ($n_L^* = 40$, $n_S^* = 156$) are cultivar-specific empirical parameters rather than universal classification criteria.
- Illumination variability. Acquisition heterogeneity. Images of the 1–3 and 4–5 month groups were captured on-tree in the orchard, whereas 6–8 month samples were photographed post-harvest at an on-site storage facility. Although no controlled lighting was employed in either setting, the difference in acquisition context may introduce systematic variation in background texture and illumination angle that cannot be fully disentangled from maturity-related morphological differences in the present dataset.
- Manual preprocessing. Images required manual cropping to 600×600 pixels. This step introduces operator dependency and limits throughput in practical deployments.
- Processing time. The mean processing time of 57 seconds per image precludes real-time field deployment in the current implementation, as discussed in section 3.
- 2D projection. Analysis of the curved peel surface from a 2D image introduces potential geometric distortion in density and distance measurements, particularly for samples with pronounced surface curvature.

These constraints reflect common challenges in transitioning image-based sensing from controlled laboratory conditions to practical orchard environments [1], [16].

4.4. Future work

Three directions are prioritised for future investigation. First, dataset expansion across multiple Khao Yai orchards and additional Citrus maxima cultivars is required to assess the generalisability of the derived thresholds and to support statistically robust threshold optimisation. Point-pattern diagnostic approaches could be applied to characterise inter-gland spatial distributions more rigorously across cultivars [24].

Second, automated region-of-interest extraction through semantic segmentation would eliminate the current manual cropping dependency, enabling higher throughput and reducing operator variability [25]. Integration of illumination normalisation or colour constancy preprocessing could further improve binarization robustness under variable field conditions [16].

Third, computational optimisation of the multi-scale detection stage — the primary bottleneck at the current processing rate of 57 seconds per image — represents a necessary step toward practical deployment. Kernel parallelisation or replacement of the exhaustive multi-pass strategy with a single-pass learned detector could substantially reduce processing time. Deployment on dedicated embedded vision hardware has been demonstrated as feasible for comparable citrus sorting applications [26], providing a practical deployment pathway for a rule-based pipeline of the type proposed here.

5. CONCLUSION

This study investigated the feasibility of oil-gland morphology as an interpretable, non-destructive maturity indicator for pomelo (*Citrus maxima*, Khao Yai cultivar) using a rule-based image-processing pipeline. The pipeline achieved an overall accuracy of 78.79% and a macro-averaged F1-score of 0.784 on a balanced dataset of 33 field-acquired samples ($n = 11$ per stage). Synthetic dot-pattern validation confirmed a detection rate of 96.1%, establishing algorithmic reliability independently of biological variability. No misclassification occurred between the most developmentally distinct groups (1–3 and 6–8 months), indicating that the pipeline correctly captures the principal oil-gland developmental contrast during pomelo maturation.

The framework requires no model training, labelled datasets, or specialist imaging hardware, operating on consumer-grade RGB images captured under natural illumination. These characteristics distinguish it from spectroscopic and deep-learning approaches that depend on controlled conditions or extensive training data.

The findings are interpreted as methodological feasibility rather than validated generalisation. The empirical thresholds and morphological patterns reported here are specific to the Khao Yai cultivar under the described acquisition conditions and establish a quantitative baseline for future multi-cultivar, multi-orchard investigations of morphology-based maturity assessment in pomelo.

ACKNOWLEDGMENTS

The authors would like to express their sincere gratitude to Kiattisak Naria, for his dedicated contribution as a research assistant.

FUNDING INFORMATION

This work was supported by the Advanced Signal Processing for Disruptive Innovation Research Center, Nakhon Pathom Rajabhat University.

AUTHOR CONTRIBUTIONS STATEMENT

This journal uses the Contributor Roles Taxonomy (CRediT) to recognize individual author contributions, reduce authorship disputes, and facilitate collaboration.

Name of Author	C	M	So	Va	Fo	I	R	D	O	E	Vi	Su	P	Fu
Sopapun Suwansawang	✓	✓	✓	✓	✓	✓			✓	✓	✓	✓	✓	✓
Harutai Dinsakul	✓	✓		✓		✓	✓	✓		✓			✓	
Wirot Buangam				✓		✓	✓			✓				
Jiraroj Tosasukul		✓	✓	✓	✓			✓		✓				

C : **C**onceptualization
M : **M**ethodology
So : **S**oftware
Va : **V**alidation
Fo : **F**ormal Analysis
I : **I**nvestigation
R : **R**esources
D : **D**ata Curation
O : Writing - **O**riginal Draft
E : Writing - Review & **E**diting
Vi : **V**isualization
Su : **S**upervision
P : **P**roject Administration
Fu : **F**unding Acquisition

CONFLICT OF INTEREST STATEMENT

The authors state no conflict of interest.

DATA AVAILABILITY

The data that support the findings of this study, and implementation details beyond those provided in Algorithm 1 and sections 2.1–2.4, are available from the corresponding authors upon reasonable request.

REFERENCES

[1] J. Ma, M. Li, W. Fan, and J. Liu, "State-of-the-art techniques for fruit maturity detection," *Agronomy*, vol. 14, no. 12, p. 2783, Nov. 2024, doi: 10.3390/agronomy14122783.

[2] X. Zhou, X. Hu, and J. Sun, "A review of fruit ripeness recognition methods based on deep learning," *Cyber-Physical Systems*, vol. 11, no. 4, pp. 508–542, Oct. 2025, doi: 10.1080/23335777.2025.2467639.

[3] I. R. Santelices, S. Cano, F. Moreira, and Á. P. Fritz, "Artificial vision systems for fruit inspection and classification: systematic literature review," *Sensors*, vol. 25, no. 5, p. 1524, Feb. 2025, doi: 10.3390/s25051524.

[4] R. Singh, C. Nickhil, K. Upendar, P. Mishra, and S. C. Deka, "Deep learning-based approach for classifying mandarin orange maturity," *Sustainable Food Technology*, vol. 3, no. 6, pp. 2215–2225, 2025, doi: 10.1039/d5fb00408j.

[5] I. Esaki, S. Noma, T. Ban, R. Sultana, and I. Shimizu, "Maturity classification of blueberry fruit using YOLO and vision transformer for agricultural assistance," *Horticulturae*, vol. 11, no. 10, p. 1272, Oct. 2025, doi: 10.3390/horticulturae11101272.

[6] M. Winklmair, R. Sekulic, J. Kraus, P. Penava, and R. Buettner, "A deep learning based approach for classifying the maturity of cashew apples," *Plos One*, vol. 20, no. 6 June, p. e0326103, Jun. 2025, doi: 10.1371/journal.pone.0326103.

[7] J. Hongwiangjan, A. Terdwongworakul, and K. Krisanapook, "Evaluation of pomelo maturity based on acoustic response and peel properties," *International Journal of Food Science and Technology*, vol. 50, no. 3, pp. 782–789, Mar. 2015, doi: 10.1111/ijfs.12700.

[8] S. S. Voo, H. D. Grimes, and M. B. Lange, "Assessing the biosynthetic capabilities of secretory glands in citrus peel," *Plant Physiology*, vol. 159, no. 1, pp. 81–94, May 2012, doi: 10.1104/pp.112.194233.

[9] K. Peng, W. Ma, J. Lu, Z. Tian, and Z. Yang, "Application of machine vision technology in citrus production," *Applied Sciences (Switzerland)*, vol. 13, no. 16, p. 9334, Aug. 2023, doi: 10.3390/app13169334.

[10] S. Gao *et al.*, "Non-destructive storage time prediction of newhall navel oranges based on the characteristics of rind oil glands," *Frontiers in Plant Science*, vol. 13, Mar. 2022, doi: 10.3389/fpls.2022.811630.

[11] K. Phuangsombut, A. Phuangsombut, and A. Terdwongworakul, "Combination of visible reflectance and acoustic response to improve non-destructive assessment of maturity and indirect prediction of internal quality of red-fleshed pomelo," *International Journal of Food Science and Technology*, vol. 56, no. 2, pp. 936–944, Feb. 2021, doi: 10.1111/ijfs.14746.

[12] F. Xiao, H. Wang, Y. Li, Y. Cao, X. Lv, and G. Xu, "Object detection and recognition techniques based on digital image processing and traditional machine learning for fruit and vegetable harvesting robots: an overview and review," *Agronomy*, vol. 13, no. 3, p. 639, Feb. 2023, doi: 10.3390/agronomy13030639.

[13] D. Bradley and G. Roth, "Adaptive thresholding using the integral image," *Journal of Graphics Tools*, vol. 12, no. 2, pp. 13–21, Jan. 2007, doi: 10.1080/2151237X.2007.10129236.

[14] R. C. Gonzalez and R. E. Woods, *Digital Image Processing*, 4th ed. New York, 2018.

[15] T. Lindeberg, "Scale-space theory: a basic tool for analyzing structures at different scales," *Journal of Applied Statistics*, vol. 21, no. 1–2, pp. 225–270, Jan. 1994, doi: 10.1080/757582976.

[16] C. Wang, Q. Han, C. Li, T. Zou, and X. Zou, "Fusion of fruit image processing and deep learning: a study on identification of citrus ripeness based on R-LBP algorithm and YOLO-CIT model," *Frontiers in Plant Science*, vol. 15, Jun. 2024, doi: 10.3389/fpls.2024.1397816.

[17] N. Otsu, "A threshold selection method from gray-level histograms," *IEEE Transactions on Systems, Man and Cybernetics*, vol. 9, no. 1, pp. 62–66, 1996, [Online]. Available: https://cw.fel.cvut.cz/b201/_media/courses/a6m33bio/otsu.pdf.

[18] L. He, X. Ren, Q. Gao, X. Zhao, B. Yao, and Y. Chao, "The connected-component labeling problem: a review of state-of-the-art algorithms," *Pattern Recognition*, vol. 70, pp. 25–43, Oct. 2017, doi: 10.1016/j.patcog.2017.04.018.

[19] E. J. Amézquita, M. Y. Quigley, T. Ophelders, D. Seymour, E. Munch, and D. H. Chitwood, "The shape of aroma: measuring and modeling citrus oil gland distribution," *Plants People Planet*, vol. 5, no. 5, pp. 698–711, Sep. 2023, doi: 10.1002/ppp3.10333.

[20] M. Sokolova and G. Lapalme, "A systematic analysis of performance measures for classification tasks," *Information Processing and Management*, vol. 45, no. 4, pp. 427–437, Jul. 2009, doi: 10.1016/j.ipm.2009.03.002.

[21] J. Opitz and S. Burst, "Macro F1 and Macro F1," *arXiv preprint arXiv:1911.03347*, 2019, [Online]. Available: http://arxiv.org/abs/1911.03347

[22] D. Chicco and G. Jurman, "The advantages of the Matthews correlation coefficient (MCC) over F1 score and accuracy in binary classification evaluation," *BMC Genomics*, vol. 21, no. 1, p. 6, Dec. 2020, doi: 10.1186/s12864-019-6413-7.

[23] A. Agresti, Categorical Data Analysis, 3rd ed. Hoboken, 2013.

[24] A. Baddeley, E. Rubak, and R. Turner, *Spatial Point Patterns: Methodology and Applications with R. Boca Raton*, Boca Raton: FL: Chapman and Hall/CRC, 2015.

[25] M. A. Nuño-Maganda *et al.*, "Real-time embedded vision system for online monitoring and sorting of citrus fruits," *Electronics (Switzerland)*, vol. 12, no. 18, p. 3891, Sep. 2023, doi: 10.3390/electronics12183891.

[26] O. Ronneberger, P. Fischer, and T. Brox, "U-net: convolutional networks for biomedical image segmentation," in *Lecture Notes in Computer Science (including subseries Lecture Notes in Artificial Intelligence and Lecture Notes in Bioinformatics)*, vol. 9351, 2015, pp. 234–241. doi: 10.1007/978-3-319-24574-4_28.

BIOGRAPHIES OF AUTHORS

Sopapun Suwansawang received the Ph.D. degree in Electronic Engineering from the University of York, United Kingdom. She is currently an assistant professor at the Department of Electrical Engineering, Nakhon Pathom Rajabhat University, Thailand. Her research expertise and interests focus on computational neuroscience, signal processing, and computer vision. He can be contacted at email: sopapun@webmail.npru.ac.th.

Harutai Dinsakul received the M.Eng. degree in Electrical Engineering from King Mongkut's University of Technology North Bangkok, Thailand. She is currently an assistant professor with the Electronic Engineering Program, Department of Electrical Engineering, Faculty of Science and Technology, Nakhon Pathom Rajabhat University, Thailand. Her research interests include IoT technologies, embedded systems design, and smart farming applications in agricultural engineering. She can be contacted at email: harutai@webmail.npru.ac.th.

Wirot Buangam received the M.Eng. degree in Electrical Engineering from King Mongkut's University of Technology North Bangkok, Thailand. He is currently an assistant professor with the Department of Electrical Engineering, Faculty of Science and Technology, Nakhon Pathom Rajabhat University, Thailand. His research interests include embedded systems design, machine learning, and agricultural engineering. He can be contacted at email:wirot@npru.ac.th.

Jiraroj Tosasukul received the Ph.D. degree in Mathematics from the University of York, United Kingdom. He is currently an assistant professor of Statistics and Data Science with the Department of Mathematics, Naresuan University, Thailand. His research interests include machine learning, high-dimensional statistics, time series forecasting, and statistical modeling. He can be contacted at email: jirarojt@nu.ac.th.